

Chemical bath deposition of $\text{Zn}_{1-x}\text{Sn}_x\text{O}_y$ films as buffer layers for $\text{Cu}(\text{In,Ga})\text{Se}_2$ solar cells

Diego A. Garzón, Christian Rossi, Ishwor Khatri, Francesco Soggia, Ihsan Çaha, Francis Leonard Deepak, Diego Colombara, Sascha Sadewasser*

D. A. Garzón, C. Rossi, I. Khatri, I. Çaha, F. L. Deepak, S. Sadewasser
International Iberian Nanotechnology Laboratory, Avenida Mestre José Veiga s/n, Braga
4715-330, Portugal.

E-mail: sascha.sadewasser@inl.int

D. A. Garzón

Departamento de Química e Bioquímica, Faculdade de Ciências, Universidade do Porto, Rua
do Campo Alegre 687, 4169-007 Porto, Portugal

C. Rossi, F. Soggia, D. Colombara, F. Soggia

Università degli Studi di Genova, Department of Chemistry and Industrial Chemistry, via
Dodecaneso 31 16146 Genova, Italy

Keywords: Buffer layer, CIGSe, Chemical bath deposition, Thin film solar cells, Zinc tin oxide.

$\text{Cu}(\text{In,Ga})\text{Se}_2$ (CIGSe) thin-film solar cells are a commercial photovoltaic technology that provides sustainable power. Here, we study the formation of $\text{Zn}_{1-x}\text{Sn}_x\text{O}_y$ (ZTO) thin films as Cd-free buffer layers by chemical bath deposition (CBD) suitable for CIGSe solar cell devices. ZTO films were obtained by CBD onto SLG, by modifying a reported procedure otherwise leading to columnar ZnO thin films. Our ZTO films show a flatter morphology compared to the reference ZnO due to inhibition of the columnar growth. In addition, a non-trivial increase of the band gap was observed by enhancing Sn concentration. When a concentration of 20% $[\text{Sn}]/([\text{Sn}]+[\text{Zn}])$ (where $[\text{Sn}]$ and $[\text{Zn}]$ are the molar concentrations of Sn and Zn, respectively) is employed in the chemical bath, the resulting buffer layer allowed the CIGSe solar cell to achieve similar performance as with a CdS buffer layer (average efficiency of $(11 \pm 2)\%$), yielding a maximum efficiency of 10.4%, with an average of $(9 \pm 2)\%$.

1. Introduction

Cu(In,Ga)Se₂ (CIGSe) thin-film solar cells present an opportunity for flexible, tandem or semi-transparent applications, together with easy and cheap manufacturing for large-area modules due to milder processing temperatures compared to silicon solar cells.¹⁻⁴ This technology has been widely studied because CIGSe can be prepared by several methods that give high control over its properties, notably its tunable band gap (1.0 - 1.7 eV)^{5,6}, and high absorption coefficient ($>10^5 \text{ cm}^{-1}$)^{5,6} with a record power conversion efficiency (PCE) of 23.4% achieved by SolarFrontier.⁷

A key component in CIGSe solar cells is the buffer layer, which forms the charge-separating pn-junction with the absorber and provides a good electrical and optical interface with the front contact layers, ensuring charge carrier transport and minimal interface recombination. CdS deposited by chemical bath deposition (CBD) is the traditional buffer material due to its electrical and structural matching with the absorber.⁸ This n-type material only yields high efficiency solar cells when it is deposited by CBD, due to the action of ammonia on the surface of CIGSe and the complete and conformal coverage over the polycrystalline CIGSe.⁹ The CBD technique consists of the deposition of inorganic (oxide, sulfide, or selenide) thin films by immersion of a substrate in a precursor solution. It is based on a controlled chemical reaction (normally a hydrolysis) performed typically in an aqueous solution that yields coating of the substrate (heterogeneous nucleation at the solution/substrate interface) while also resulting in a colloidal suspension (homogeneous nucleation occurring in solution). Generally, the precursor aqueous solution involves a soluble metal salt, a pH agent, and a complexing agent, used to control the hydrolysis rate.

However, the relatively low direct band gap of CdS, $E_g = 2.4\text{-}2.5 \text{ eV}$ ¹⁰, prevents high energy photons from being absorbed by the p-CIGSe.¹¹ In addition, the presence of toxic Cd presents health and environmental concerns.^{12,13} Therefore, wider band gap and less toxic materials have been researched to produce Cd-free CIGSe solar cells.^{11,14,15} Among these materials, zinc tin oxide ($\text{Zn}_{1-x}\text{Sn}_x\text{O}_y$, ZTO) has attracted much attention due to its non-toxicity, fast light responsivity, and tunable wide band gap. CIGSe solar cells based on ZTO buffers have resulted in PCE comparable to or even higher than CdS ones.^{8,11,14,16}

Until now, ZTO buffer layers on CIGSe solar cells have been only fabricated by atomic layer deposition (ALD) with atomically precise resolution in vacuum conditions by sequential vapor

reactions of organometallic precursors and gases. Although ALD allows excellent control over ZTO composition and assures excellent coverage,¹⁷ it is hardly scalable, time-consuming, and expensive. In contrast, the production of record CIGSe-based solar cells makes use of the CBD to produce CdS and other inorganic thin films as buffer layers.⁷ Moreover, CBD is known for being a low temperature (<100°C) process that yields conformal growth in a fast, reliable, cheap, and batch-scalable manner.^{18–20}

Studies on CBD for ZnO thin films have shown diverse nanostructured morphologies obtained by tuning parameters such as ligands, counter-ions of the metal salts, pH, temperature, and nature of the substrate.^{21,22} Furthermore, the electrical and optical properties of ZnO thin films have also been modified by doping with other metals such as aluminum, gallium, indium, etc.²³ Hence, the CBD of ZnO lends itself to relatively simple modifications in the bath, substrate or temperature to tune the thin-film composition and properties.

Here, we develop the deposition of ZTO thin films by CBD. We first study the deposition on soda lime glass (SLG) and the alloying with Sn, to understand the effect of Sn cations. Subsequently, the application as buffer layer for CIGSe-based solar cells was investigated, and we compare the current density - voltage (JV) characteristics of solar cell devices based on ZTO buffer layers with those of CdS-based CIGSe solar cells.

2. Results and discussion

The morphology of the ZTO thin films depends strongly on the Sn concentration in the bath solution (**Figure 1a**). The Sn-free ZnO thin film on SLG exhibits a columnar growth, with a preferential (002) plane orientation, also reported by Kokotov, et al.¹⁹ Surprisingly, such a columnar structure was not observed even for TTZ as low as 1%, where TTZ represents the molar ($[\text{Sn}]/([\text{Sn}]+[\text{Zn}])$) ratio in the solution. In the range 1 - 10% TTZ the morphology corresponds to truncated columns. Samples grown at 15% TTZ show a compact film, due to lateral growth constrained by the contact between neighboring crystals. Higher Sn concentrations give rise to compact films with small elongated grains. ZTO with 50% TTZ shows an almost cubic morphology, consistent with earlier reports.^{24,25} Substrates subject to 50% and higher TTZ baths show a poor coverage of the SLG, with only small regions displaying material, probably due to the high amount of homogenous nucleation in the bath (not shown).

To better understand these changes in morphology, X-ray diffraction (XRD) was performed on all films (**Figure 1b**). The addition of Sn in the solution modifies the intensity of the ZnO peaks

without introducing any additional reflection. Thus, no additional phase detectable by XRD appears to form up to 40% TTZ. It is worth to note that some of the peaks of the references are not present in the diffractograms of the samples. This inconsistency might be explained considering that the samples experience preferential orientation favored by their thin film organization while typically the references are acquired onto powders which are randomly oriented and hence do not display any preferential orientation.

However, the intensity of the peak related to the ZnO (002) plane decreases with the addition of Sn, until it is no longer visible for concentrations greater than 10% TTZ. This phenomenon has been reported for ZnO depositions where additional metals were added as well as in ZTO films deposited by ALD.³ In these cases, the charged complexes of foreign ions appear to passivate differently the crystal facets of ZnO-columns by electrostatic interactions.^{26,27} At 50 % TTZ the peaks observed correspond to reflections of the (220) and (420) planes associated to the $\text{ZnSn}(\text{OH})_6$ phase.²⁸ Thus, an oxidation of Sn from the precursor Sn(II) to the Sn(IV) present in the hydroxide phase must be occurring in the bath.

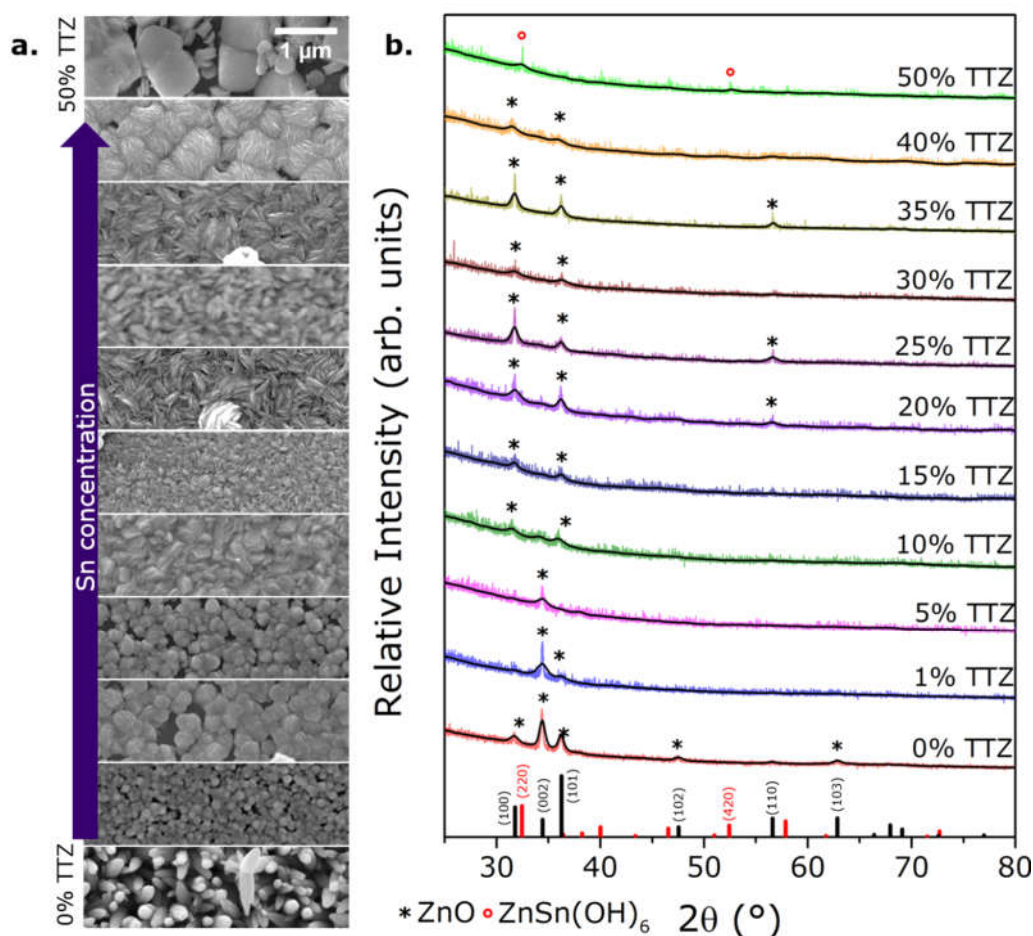


Figure 1. (a) High magnification scanning electron microscopy (SEM) images of the ZnO thin films obtained at different Sn nominal doping concentrations. (b) XRD patterns for ZTO thin films onto SLG. The black line corresponds to a fitting (HighScore software), TTZ is the molar $[\text{Sn}]/([\text{Sn}]+[\text{Zn}])$ ratio. The reference patterns at the bottom correspond to ZnO (black bars) and $\text{ZnSn}(\text{OH})_6$ (red bars).

All obtained ZTO films with TTZ up to 50% are highly transparent with transmission above 76% in the wavelength range between 500 and 1200 nm (**Figure 2a**); the reflectance and absorption spectra are shown in **Figure S1**. The band gap (**Figure 2b**), extracted from the transmittance and reflectance spectra by the Tauc method (**Figure 2c and d**), presents a non-linear increase with increasing Sn concentration, ranging between the values for ZnO (3.2 eV) and SnO_2 (3.9 eV).^{29,30} This optical behavior has been reported in ZTO films deposited by several methods, such as spray pyrolysis, magnetron sputtering, and ALD.^{31–33} This effect has been understood as a mixture of the concentration of the dopant (Sn) and changes in the microstructure of the material.³² The band gap behavior can be correlated with the changes in XRD patterns and morphology, where there were significant changes for lower TTZ films together with similar morphology in the range 20 - 40 % TTZ. The latter opens the possibility of tuning the band gap from 3.2 to 3.6 eV.

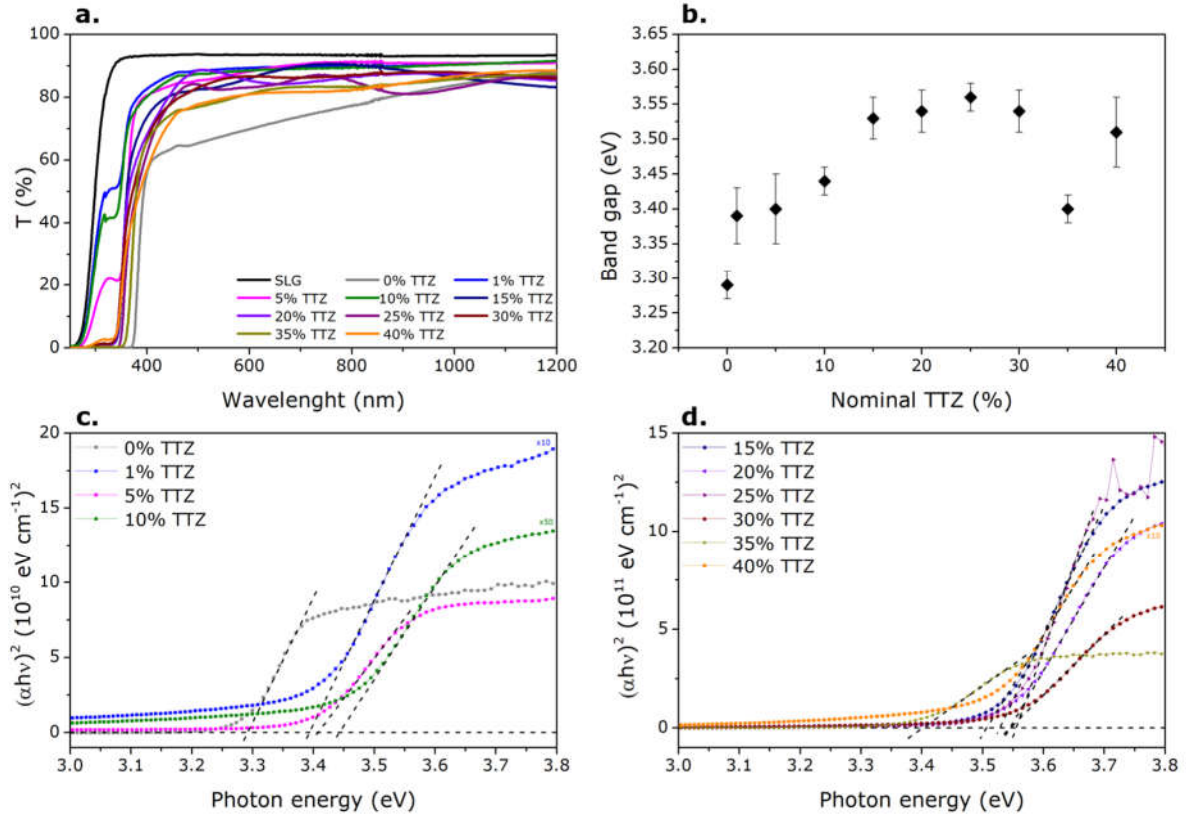


Figure 2. (a) Transmittance spectra and (b) variation of the band gap of ZTO films as a function of nominal TTZ, obtained by (c,d) extrapolation in the Tauc method.

In the following, we explore the suitability of ZTO films deposited by the developed CBD process as buffer layer for CIGSe solar cells (**Figure 3a**). The deposition of ZTO on SLG substrates required an activation step with potassium permanganate. Nevertheless, the deposition of ZTO performed directly on CIGSe yielded good thin films even without activation step. We studied concentrations between 10 and 40% TTZ and, for all concentrations, a deposition time of 30 min resulted in a thickness of (350 ± 15) nm as measured by SEM cross-section imaging (**Figure 3c, e, g, i**). As observed for the growth on SLG substrates, the change of Sn nominal concentration produces different ZTO morphologies also on CIGSe substrates (**Figure 3**). For 10% TTZ, truncated columns are observed (**Figure 3d**), whereas 20% TTZ yields a morphology with small grains elongated in parallel to the substrate (**Figure 3f**). In the case of 30% TTZ, the grains assume a spherical shape (**Figure 3h**), while for the highest concentration tested the spheres become round-edged cuboids (**Figure 3j**). In all cases, the ZTO thin films display smaller grains than the underlying CIGSe substrate (**Figure 3b**).

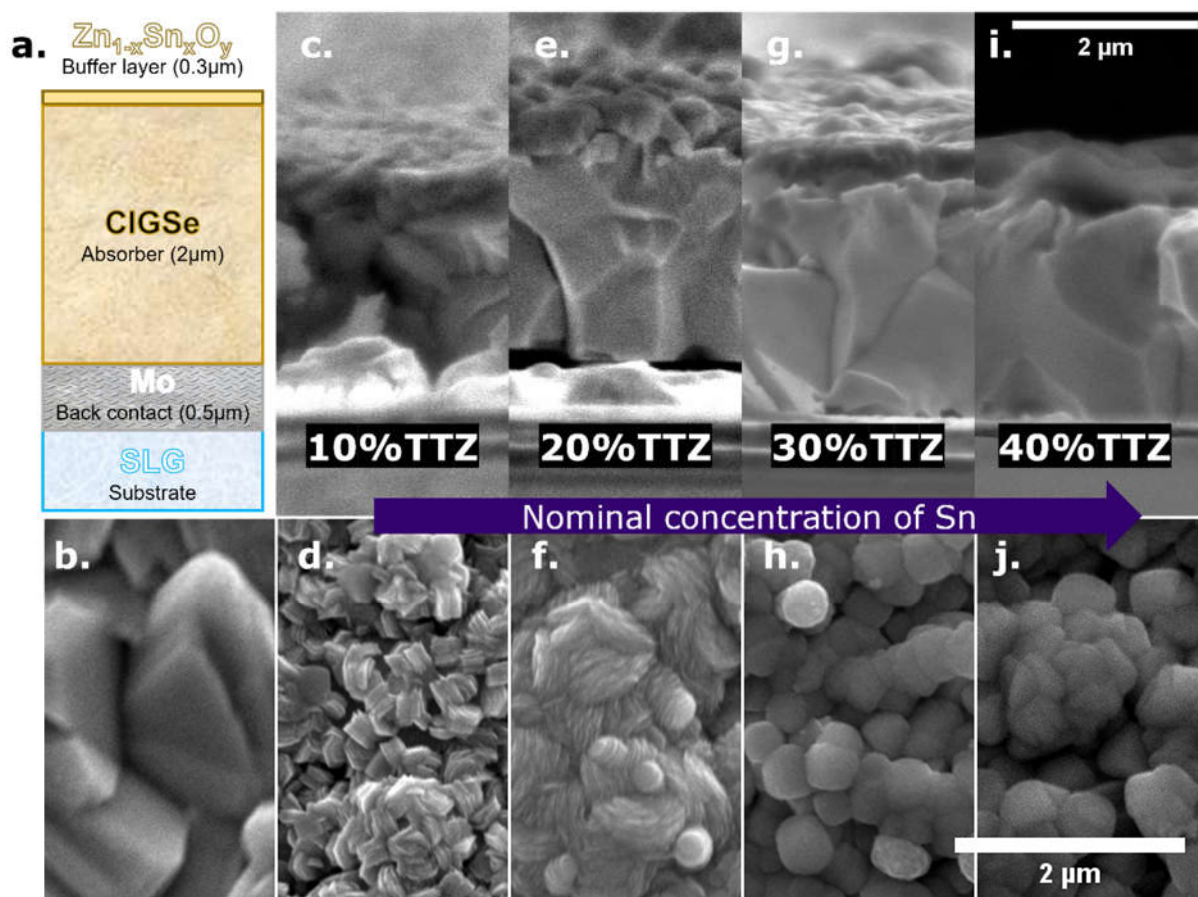


Figure 3. (a) Schematic of the SLG/Mo/CIGSe substrate used for the deposition of the ZTO thin films. (b) Top view SEM image of the CIGSe thin film. Cross-section and top-view SEM images of ZTO thin films with (c, d) 10% TTZ, (e, f) 20% TTZ, (g, h) 30% TTZ, (i, j) 40% TTZ, as grown onto CIGSe.

Quantification of the TTZ ratio in the ZTO buffer layer was performed by dissolving the respective layer in an acidic solution and measuring the concentration of Zn and Sn by inductively coupled plasma atomic emission spectroscopy (ICP-AES) (**Figure 4a**). The data show that an increase of the TTZ in the solution leads to an enhancement of the Sn content in the film. However, the incorporation of Sn into the thin films does not exhibit a simple linear dependence on the concentration in the solution. This difference may originate from the precipitation of tin oxides and hydroxides during the deposition, which competes with the incorporation of Sn in the growth of the thin film. For comparison, the TTZ of thin films deposited on Quartz is also shown, revealing that increasing Sn concentrations in solution lead to Sn-rich films, with a similar dependence as the one observed for CIGSe. This result supports the hypothesis that the precipitation of tin oxides might play a role; nevertheless, some

differences in the film TTZ (TTZ_{film}) vs. solution TTZ (TTZ) are observed, which could indicate that the substrate also plays a role in the inclusion of Sn ions into the film during the deposition.

The ZTO thin films on CIGSe were also analyzed by XPS to confirm the electronic state and composition. The survey spectra show the presence of Zn, O and Sn (**Figure S2a**) for all the studied TTZ compositions. Regarding the samples with 10 and 20% TTZ, the peak at 531 eV is related to the O²⁻ position in the wurtzite structure, while the peak at 530 eV corresponds to oxygen vacancies and/or -OH group.^{3,34-36} Furthermore, concentrations with TTZ higher than 20% show only the peak related to oxygen vacancies and/or -OH group (**Figure S2b**). Therefore, the chemical formula is conservatively identified as Zn_{1-x}Sn_xO_y.

The XPS analysis (**Figure S2c**) also shows peaks related to the spin-orbit coupling of Zn 2p_{3/2} and Zn 2p_{1/2} at 1021 eV and 1044 eV, respectively. The latter indicates a normal Zn²⁺ state with a difference between the peaks of 23 eV.^{34,37} In addition, XPS scans exhibit peaks corresponding to the spin-orbit coupling of Sn 3d_{5/2} and Sn 3d_{3/2} at 486.68 eV and 495.14 eV, respectively, and a peak corresponding to the Auger Zn L₃M₄₅M₄₅ transition at 498 - 499 eV that overlaps with the peak of Sn 3d_{3/2} (**Figure S2d**). The Sn 3d_{5/2} peak at 486.68 eV is originated by Sn⁴⁺ by comparing its peak position to the literature (**Table S1**)³⁷⁻⁴³ thus, confirming that during the bath there is an oxidation of the Sn, due to the instability of Sn(II) at alkaline pH.⁴⁴

The relative intensity of the L₃M₄₅M₄₅ signal decreases with increasing TTZ and its position shifts to higher energy when the Sn concentration is higher than or equal to 30% TTZ. It is reported that the probability of this kind of transitions is related to the morphology, which drastically changes after 30% TTZ.^{34,38} In addition, by the analysis of the Auger transition, the determination of interstitial Zn (Zn_i) and Zn-O is possible.⁴⁵ Nevertheless, in our case the overlapping of this peak with the Sn 3d_{3/2} does not allow a further understanding of the different states of Zn in the surface of the sample. Furthermore, the XPS data was also used to quantify the TTZ_{film} in the ZTO films, confirming the trends observed by ICP (**Figure 4a** and **Figure S2e**). Nevertheless, the ICP measurements correspond to the bulk TTZ, which was preferred in the following discussion.

Lastly, solar cell devices with the ZTO buffer layers were fabricated and their respective JV curves and parameters are shown in **Figure 4**, together with CdS-based reference devices. The CdS-based solar cells show a narrow distribution of PCE with an average of (11 ± 2) %, and a J_{sc} and V_{oc} of (29 ± 4) mA cm⁻² and (598 ± 9) mV, respectively. Conversely, the ZTO-based

solar cell, achieved the best efficiency for the 20% TTZ sample (9 ± 2 %) and a champion cell showing 10.4% efficiency (champion cell values are presented in **Table S2**). This performance is due to a greater J_{sc} , V_{oc} , and FF with averages of (28 ± 1) mA cm⁻², (528 ± 21) mV, and (56 ± 8) %, respectively, compared to the other ZTO-based devices. (**Figure 4**, average values presented in **Table S3**). Comparing the average values, the 20% TTZ ZTO-based devices behave similarly to the CdS-based devices for the short-circuit current, even though the ZTO buffer layer has larger thickness. The latter is related to the larger bandgap of ZTO (3.5 eV) compared to that of CdS (2.4 eV), which in principle can reduce the parasitic light absorption compared to the latter, as can be seen in the shape of the external quantum efficiency (EQE) measurement (**Figure S2f**).⁸ In addition, the EQE spectra show an oscillatory behavior in the low wavelength range for all the ZTO-based devices, which can be attributed to the reflectance (**Figure S3a**), and is significantly reduced in the internal QE (IQE) spectra (**Figure S3b**). Additionally, a gain at wavelengths greater than 900 nm is observed, which has been reported in the literature.^{17,46}

Nevertheless, the open-circuit voltage obtained for the 20% TTZ ZTO-based devices is (70 ± 23) mV less on average than the V_{oc} of the CdS devices. This decrease in the open-circuit voltage has been related to a higher surface recombination in the ZTO/CIGSe interface and a mismatch in the band alignment.^{3,47} Nevertheless, in the present case, a slightly lower effective bandgap (by ~ 50 meV, according to the EQE data in Figure S2f) of the ZTO-based devices might also contribute to their lower V_{oc} .

Additionally, the FF for the 20% TTZ ZTO-based devices is lower than the CdS reference. This comes, in part, from the lower open-circuit voltage, which affects the FF by an empirical expression.^{47,48} Moreover, the ZTO-based solar cells exhibit a higher series resistance that has a negative impact on the FF and is related to the poor conductivity of ZTO thin films and the relatively large thickness of the studied buffer layers, compared to the CdS reference. The latter has been already reported for CIGSe solar cells with ZTO deposited by ALD.^{3,8,47}

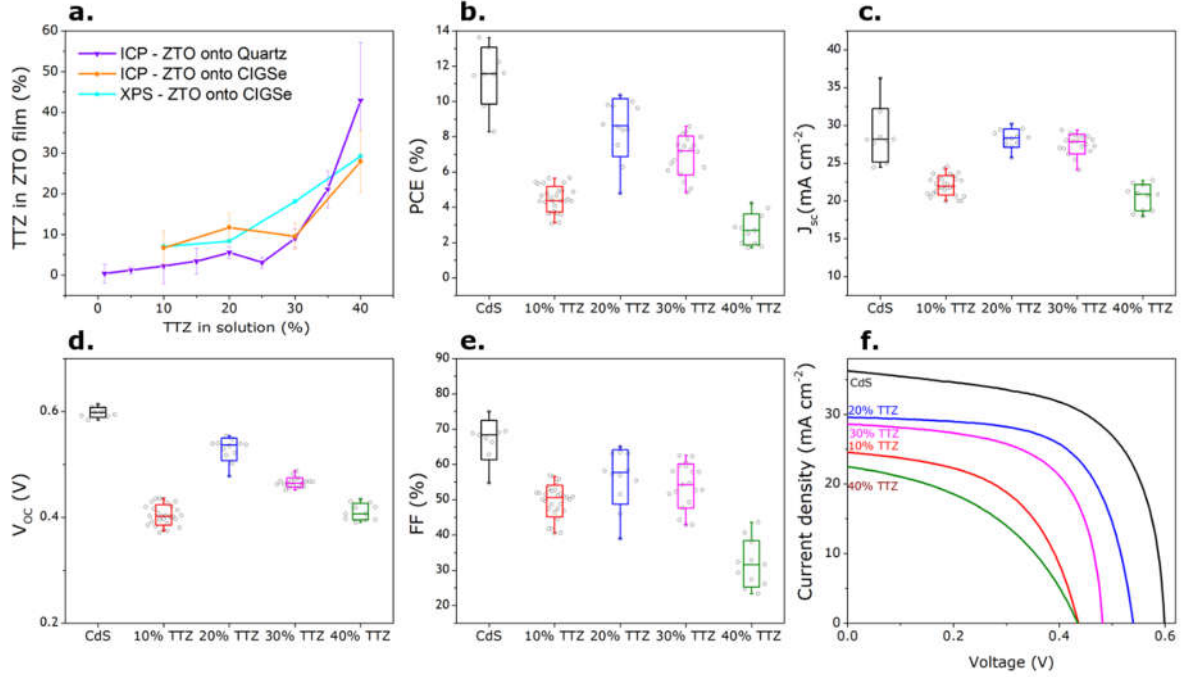


Figure 4. (a) Measured TTZ in the ZTO thin film on CIGSe and Quartz by XPS and ICP as a function of nominal TTZ in the bath solution. Solar cell parameters for CdS-based and ZTO-based devices with different compositions of ZTO buffer layers: (b) power conversion efficiency, (c) short-circuit current density, (d) open-circuit voltage, and (e) fill factor. (f) JV curves under illumination for the solar cells with CdS and ZTO buffer layers.

According to the ICP measurements, the TTZ_{film} in the ZTO film is around 10-12% for the TTZ of 20 and 30%, for which the better-performing solar cells were obtained. For the samples with 10% and 40% TTZ, the resulting solar cells show significantly poorer performance. The corresponding ZTO films have TTZ_{film} of 8 and 28%, respectively, according to the ICP analysis. These observations are in good agreement with reports in the literature where TTZ values in the range of 15-21% gave the best performance.^{8,46} The wider distribution for all the parameters in the ZTO-based devices could be related to inhomogeneities present in the p-n junction, possibly originating from the unstirred deposition bath.

It is noteworthy that the ZTO-buffered solar cells exhibit excellent performance, despite the large thickness of this buffer layer (~350 nm) compared to the standard CdS buffer layer (~50 nm). Therefore, we further investigated the ZTO buffer layer by high-resolution transmission electron microscopy (HRTEM) imaging (**Figure 5**). Specifically, the high-angle annular dark-field scanning transmission electron microscopy (HAADF-STEM) images and elemental maps are compared for the best and worst performing ZTO-based solar cell devices, i.e. for 20% and

40% TTZ, respectively. Surprisingly, the ZTO film presents inhomogeneities with Zn-poor and Sn-rich regions close to the ZTO/CIGSe interface for both 20 and 40% TTZ devices. The 40% TTZ ZTO-based device exhibits a greater quantity of these Zn-poor Sn-rich regions (**Figure S4**) which also cover the full thickness of the ZTO film in some places (**Figure 5 e-h**). The elemental maps of selenium are displayed to indicate the position of the ZTO/CIGSe interface

After an elemental quantification by energy-dispersive X-ray spectroscopy (EDS) (**Figure S5**), the darker (in the HAADF image) Sn-rich regions for both devices present an average of $(33 \pm 4) \% \text{ TTZ}_{\text{film}}$, while the brighter regions exhibit a $(3.1 \pm 0.5) \% \text{ TTZ}_{\text{film}}$. These results obtained by STEM agree with the reported TTZ_{film} by ICP, where a higher TTZ_{film} is related to higher TTZ, due to the existence of more Sn-rich regions. It seems that the presence of too many Sn-rich regions can deteriorate drastically the performance of the solar cell, whereas a small number of Sn-rich regions at the interface, as in the case of the 20% TTZ ZTO-based device, gives the best performance compared to the CdS reference. The latter feature could be related to point-contact-like passivation of the interface, which would decrease the charge carrier recombination in the Sn-rich regions, as has been reported for nanostructured buffer layers.^{49,50} Further investigation regarding the interface of ZTO/CIGSe is needed to fully understand the role of these Sn-rich regions.

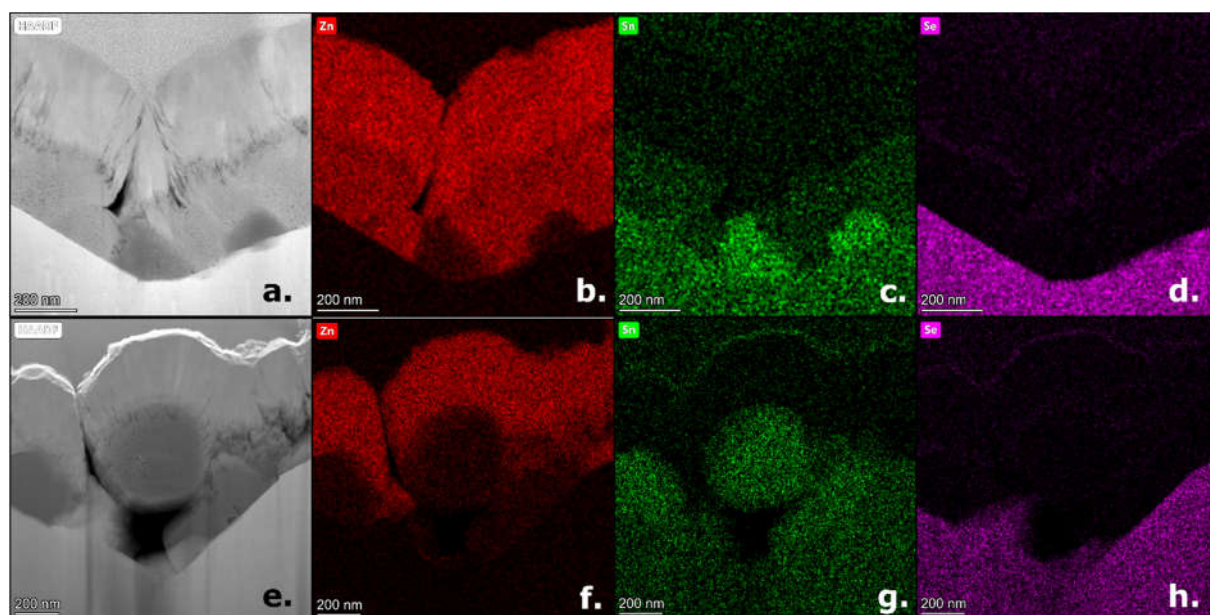


Figure 5. HAADF-STEM images of the ZTO-CIGSe solar cells: (a) ZTO buffer layer with 20% TTZ, (b-d) corresponding elemental maps from the area of the HAADF image for Zn (red), Sn (green), Se (violet) acquired by EDS, respectively; (e) ZTO buffer layer with 40% TTZ and (f-h) corresponding elemental maps from the area of the HAADF image for Zn, Sn and Se.

3. Conclusions

ZTO thin films were obtained by the addition of Sn cations during the chemical bath deposition of ZnO thin films onto soda-lime glass. These cations and their respective complexes in solution affect the growth of the film by electrostatic interactions via the occupation of specific crystallographic sites at the surface of the ZnO wurtzite structure. The resulting films display highly diverse final morphologies. The addition of Sn allows tuning the band gap from 3.2 eV to 3.6 eV. CIGSe solar cells with a ZTO buffer layer prepared with a TTZ of 20% (corresponding to $11.7 \pm 0.6\%$ TTZ_{film}, as measured by ICP) show a maximum efficiency of 10%, nearly matching CdS-based reference devices, with an average of $(11 \pm 2)\%$. STEM images revealed compositional inhomogeneities with Sn-rich regions close to the ZTO/CIGSe interface. However, a higher density of these Sn-rich regions, obtained for higher TTZ, deteriorates drastically the performance of respective solar cells, as in the case of the 40% TTZ ZTO buffer layer. Further investigation is required to understand the role of the Sn-rich regions at the absorber/buffer interface. Overall, ZTO thin films obtained by CBD are a viable and non-toxic alternative to CdS-based CIGSe solar cells with comparable PCE.

4. Experimental Section

Deposition of zinc tin oxide (ZTO) thin films onto soda-lime glass (SLG): Zinc tin oxide thin films were deposited onto SLG by chemical bath deposition (CBD) based on the process reported by Kokotov, et al.¹⁹ Substrates were cleaned by sonication with deionized water (DIW) and soap. Then, the SLG was activated with a fresh solution of potassium permanganate 5 mM and 25 μ L of 1-butanol per 10 mL of solution at 85°C for 20 min. The deposition bath was prepared by the consecutive addition of aliquots of ZnSO₄, NH₄OH, ethanolamine and SnCl₂ stock solutions to obtain a final concentration of 75 mM of cations ($[\text{Zn}^{2+}] + [\text{Sn}^{2+}]$), 0.2 M NH₄OH, and 1.6 M ethanolamine. The depositions were carried out at 92 °C with a variation of the $[\text{Sn}]/([\text{Sn}] + [\text{Zn}])$ ratio (TTZ) for 10-70 min in a range of 0-50 % TTZ by adding different aliquots of stock solutions of ZnSO₄ and SnCl₂. The stock solution of tin (II) chloride 1.5 M was prepared in an acidic medium with sufficient concentrated HCl to obtain a clear solution (~ 1.7 M HCl), the latter to prevent the hydrolysis and precipitation of tin hydroxides. Moreover, a solid precipitates during the deposition, due to the formation of tin oxides and hydroxides.

Fabrication of thin-film solar cells: For the solar cell fabrication, industry-grade CIGSe absorbers supplied by Nice Solar GmbH were employed. These absorbers have shown a PCE of 15.6%.⁵¹ They are composed of a soda-lime glass substrate with a thin layer (500 nm) of

molybdenum as back contact and a layer of around 2-3 μm of CIGSe on top. Nevertheless, for a fair comparison among the two buffer layers, we treated the CIGSe with a fresh 5 wt. % KCN solution for 1 min to remove any Cu-selenides and to refresh the surface.^{52,53} Immediately after the etching, the buffer layer (CdS or ZTO) was deposited by CBD. In the case of 50 nm thick CdS deposition, a solution of 1.33 g of thiourea, 0.13 g of cadmium acetate, 15 ml of NH_4OH , and 115 ml of DIW were used.⁵⁴ The bath was prepared by the sequential addition of DIW, NH_4OH , $\text{Cd}(\text{CH}_3\text{CO}_2)_2$ and thiourea; it was set at 60 °C and the sample was immersed for 7 min. For the ZTO buffer, the same protocol described above was used, but without activation of the substrate and with a deposition time of 30 min at 92°C. In this case, a range of 10 – 40 % TTZ was investigated.

To complete the solar cells, a double window layer was deposited by radio-frequency (RF) sputtering at room temperature in the window chamber of the Sputtering for Advanced Research (STAR) system.⁵¹ Firstly, an intrinsic ZnMgO layer was deposited at 6.1×10^{-3} mbar Ar pressure with 50 W for 14 min (thickness around 20 nm) and finally, an aluminum-doped ZnO layer was deposited at 4.0×10^{-3} mbar Ar pressure with 59 W for 51.5 min (~300 nm).

Films and device characterization: The thin-film morphology was determined by top-view and cross-section micrographs obtained by scanning electron microscopy (SEM) in an FEI Quanta 50 FEG SEM and a dual-beam FEI Helios focused ion beam (FIB). The optical transmittance and reflectance of the thin films on SLG were measured in the range of 250-1200 nm with a PerkinElmer LAMBDA 950 UV-VIS-NIR spectrophotometer coupled with an integrating sphere detector module. The optical band gaps were determined by the Tauc method considering multiple internal reflections in a thin film⁵⁵, where the band gap is equal to the abscissa of $(\alpha h\nu)^r$ as a function of photon energy ($h\nu$), with $r=2$ (for direct band gap materials), $\alpha = (\ln((1-R)^2/T + ((1-R)^4/4T^2) + R^2)^{0.5})/t$, with T = the measured transmittance, R = the measured reflectance, and t = the film thickness.⁵⁶ The thickness of the samples was assessed by contact profilometry with the Tencor P-16 Surface Profiler.

The crystal structure was determined by X-ray diffraction (XRD) using $\text{Cu K}\alpha$ radiation in a Panalytical XPert PRO MRD. The XRD patterns were processed in HighScore, and the patterns shown corresponds to the raw data and a fitting. The chemical composition of the thin films was determined by X-Ray photoelectron spectroscopy (XPS) with the ESCALAB 250Xi (Thermo Scientific). Firstly, an XPS survey was performed followed by high-resolution scans for C 1s, O 1s, Sn 3d, and Zn 2p. Lastly, the peaks were fitted and the TTZ_{film} was determined

with the areas related to the Zn 2p_{3/2} and Sn 3d_{5/2}. The C 1s peak (284.8 eV) was used as an internal standard for binding energy calibration.

Furthermore, a Varian (Springvale, Australia) Vista PRO ICP-AES with a sample introduction system consisting of a glass concentric K-style pneumatic nebulizer jointed to a glass cyclonic spray chamber was employed for the determination of TTZ_{film}. All samples were analyzed 7 times using on-line internal standardization (10 mg/L Lu standard solution).

ZTO-based solar cells were analyzed by scanning transmission electron microscopy (STEM) and energy dispersive spectroscopy (EDS). These studies were carried out with a double-corrected FEI Titan G3 Cubed Themis equipped with a Super-X EDX System, operated at 200 kV. The samples for STEM/EDS analysis were prepared by a dual-beam FEI Helios focused ion beam (FIB) following the standard lift-out procedure. In order not to destroy the outer layers by Ga⁺ ions during the milling steps, two Pt layers were deposited: ~200 nm by electron (e⁻) beam and ~2 μm by ion (i⁻) beam. 30 kV ion beam was performed for the bulk milling and thereafter the lamellae were thinned down to 100 nm in thickness. Finally, a 5 kV ion beam was used to remove the surface amorphization.

The current density - voltage (JV) characteristics of solar cell devices were measured in a solar simulator (Oriel Sol3A class AAA) under AM1.5 illumination. Devices were manually scribed to ~0.15 cm² and measured without a front grid at room temperature. External quantum efficiency (EQE) was measured by the QEX10 Solar Cell Quantum Efficiency Measurement (PV measurement Inc.). A 75 W Xenon arc lamp was used as a white light source to generate a monochromatic beam. The DC mode was used in a spectral range of 300–1100 nm. In addition, internal quantum efficiency (IQE) spectra was calculated based on the EQE and the reflectance of the solar cells measured by UV-Vis NIR spectrophotometry with an integrated sphere detector module.

Supporting Information

Supporting Information is available below.

Acknowledgements

D. A. G. acknowledges the support of the Erasmus+: Erasmus Mundus program of the European Union. We acknowledge support by the projects “Semi-TranspARent SOLAR cells for building integrated photovoltaics (STAR-SOL)” (FCT - FNR/0001/2018) and “Designing superior

CIGSe solar cells through understanding and controlling growth (Design-Solar)” (PTDC/CTM-CTM/2241/2021), both funded by FCT - Fundação para a Ciência e a Tecnologia, and by the project “Reusable Mask Patterning (REMAP), funded by the European Union under the European Innovation Council Pathfinder Open scheme (grant no. 101046909). I.K. acknowledges funding through the H2020 MSCA-IF fellowship UL-Flex-Cell (grant no. 889512). Views and opinions expressed are however those of the author(s) only and do not necessarily reflect those of the European Union or of the European Innovation Council. Neither the European Union nor the granting authority can be held responsible for them. D.C. and C.R. also acknowledge the contribution of the University of Genova through Compagnia di San Paolo foundation under the scheme “Promoting Competitiveness”.

References

- (1) Lee, T. D.; Ebong, A. U. A Review of Thin Film Solar Cell Technologies and Challenges. *Renew. Sustain. Energy Rev.* **2017**, *70*, 1286–1297. <https://doi.org/10.1016/j.rser.2016.12.028>.
- (2) Ramanujam, J.; Bishop, D. M.; Todorov, T. K.; Gunawan, O.; Rath, J.; Nekovei, R.; Artegiani, E.; Romeo, A. Flexible CIGS, CdTe and a-Si:H Based Thin Film Solar Cells: A Review. *Prog. Mater. Sci.* **2020**, *110*, 100619. <https://doi.org/10.1016/j.pmatsci.2019.100619>.
- (3) Agbenyeke, R. E.; Song, S.; Park, B. K.; Kim, G. H.; Yun, J. H.; Chung, T.-M.; Kim, C. G.; Han, J. H. Band Gap Engineering of Atomic Layer Deposited $\text{Zn}_x\text{Sn}_{1-x}\text{O}$ Buffer for Efficient $\text{Cu}(\text{In,Ga})\text{Se}_2$ Solar Cell. *Prog. Photovolt. Res. Appl.* **2018**, *26* (9), 745–751. <https://doi.org/10.1002/pip.3012>.
- (4) Fonoll-Rubio, R.; Placidi, M.; Hoelscher, T.; Thomere, A.; Li-Kao, Z. J.; Guc, M.; Izquierdo-Roca, V.; Scheer, R.; Pérez-Rodríguez, A. Characterization of the Stability of Indium Tin Oxide and Functional Layers for Semitransparent Back-Contact Applications on $\text{Cu}(\text{In,Ga})\text{Se}_2$ Solar Cells. *Sol. RRL* **2022**, *6* (7), 2101071. <https://doi.org/10.1002/solr.202101071>.
- (5) Mirabi, E.; Akrami Abarghuie, F.; Arazi, R. Integration of Buildings with Third-Generation Photovoltaic Solar Cells: A Review. *Clean Energy* **2021**, *5* (3), 505–526. <https://doi.org/10.1093/ce/zkab031>.
- (6) Ashok, A.; Narro-Rios, J. S.; Nwakanma, O.; Regmi, G.; Velumani, S.; Pulgarin-Agudelo, F. A. Characterizations of a Selenized $\text{Cu}(\text{In}_{1-x}\text{Ga}_x)\text{Se}_2$ Thin Film Absorber Layer Fabricated By a Three-Stage Hybrid Method. In *2018 15th International Conference on Electrical Engineering, Computing Science and Automatic Control (CCE)*; IEEE: Mexico City, 2018; pp 1–6. <https://doi.org/10.1109/ICEEE.2018.8533902>.
- (7) Nakamura, M.; Yamaguchi, K.; Kimoto, Y.; Yasaki, Y.; Kato, T.; Sugimoto, H. Cd-Free $\text{Cu}(\text{In,Ga})(\text{Se,S})_{2\delta}$ Thin-Film Solar Cell With Record Efficiency of 23.35%. *IEEE J Photovolt.* **2019**, *9* (6), 1863–1867. <https://doi.org/10.1109/JPHOTOV.2019.2937218>.
- (8) Lindahl, J.; Wätjen, J. T.; Hultqvist, A.; Ericson, T.; Edoff, M.; Törndahl, T. The Effect of $\text{Zn}_{1-x}\text{Sn}_x\text{O}_y$ Buffer Layer Thickness in 18.0% Efficient Cd-Free $\text{Cu}(\text{In,Ga})\text{Se}_2$ Solar

- Cells. *Prog. Photovolt. Res. Appl.* **2013**, *21* (8), 1588–1597.
<https://doi.org/10.1002/pip.2239>.
- (9) Barreau, N.; Frelon, A.; Lepetit, T.; Gautron, E.; Gautier, N.; Ribeiro-Andrade, R.; Nicoara, N.; Sadewasser, S.; Zabierowski, P.; Arzel, L.; Choubrac, L.; Harel, S.; Deudon, C.; Latouche, C.; Jobic, S.; Caldes, M.; Assmann, L.; Tsoulka, P.; Péan, E. V.; Lorthioir, J.; Geschier, F.; Braems, I.; Moret, M.; Briot, O.; Ouvrard, G. High Efficiency Solar Cell Based on Full PVD Processed Cu(In,Ga)Se₂/CdIn₂S₄ Heterojunction. *Sol. RRL* **2017**, *1* (11), 1700140. <https://doi.org/10.1002/solr.201700140>.
 - (10) Doña, J. M.; Herrero, J. Dependence of Electro-optical Properties on the Deposition Conditions of Chemical Bath Deposited CdS Thin Films. *J Electrochem Soc* **1997**, *144* (11), 4091–4098. <https://doi.org/10.1149/1.1838141>.
 - (11) Salomé, P. M. P.; Keller, J.; Törndahl, T.; Teixeira, J. P.; Nicoara, N.; Andrade, R.-R.; Stroppa, D. G.; González, J. C.; Edoff, M.; Leitão, J. P.; Sadewasser, S. CdS and Zn_{1-x}Sn_xO_y Buffer Layers for CIGS Solar Cells. *Sol. Energy Mater. Sol. Cells* **2017**, *159*, 272–281. <https://doi.org/10.1016/j.solmat.2016.09.023>.
 - (12) Haider, F. U.; Liqun, C.; Coulter, J. A.; Cheema, S. A.; Wu, J.; Zhang, R.; Wenjun, M.; Farooq, M. Cadmium Toxicity in Plants: Impacts and Remediation Strategies. *Ecotoxicol. Environ. Saf.* **2021**, *211*, 111887. <https://doi.org/10.1016/j.ecoenv.2020.111887>.
 - (13) Tokumoto, M.; Lee, J.-Y.; Satoh, M. Transcription Factors and Downstream Genes in Cadmium Toxicity. *Biol. Pharm. Bull.* **2019**, *42* (7), 1083–1088. <https://doi.org/10.1248/bpb.b19-00204>.
 - (14) Lindahl, J.; Keller, J.; Donzel-Gargand, O.; Szaniawski, P.; Edoff, M.; Törndahl, T. Deposition Temperature Induced Conduction Band Changes in Zinc Tin Oxide Buffer Layers for Cu(In,Ga)Se₂ Solar Cells. *Sol. Energy Mater. Sol. Cells* **2016**, *144*, 684–690. <https://doi.org/10.1016/j.solmat.2015.09.048>.
 - (15) Rasouli, F.; Madani, M. R. Analysis of CIGS-Based Thin Film Tandem Solar Cell with ZnS Buffer Layers. *Opt Quant Electron* **2020**, *52* (11), 481. <https://doi.org/10.1007/s11082-020-02590-4>.
 - (16) Larsson, F.; Nilsson, N. S.; Keller, J.; Frisk, C.; Kosyak, V.; Edoff, M.; Törndahl, T. Record 1.0 V Open-Circuit Voltage in Wide Band Gap Chalcopyrite Solar Cells. *Prog. Photovolt. Res. Appl.* **2017**, *25* (9), 755–763. <https://doi.org/10.1002/pip.2914>.
 - (17) Hultqvist, A.; Platzer-Björkman, C.; Zimmermann, U.; Edoff, M.; Törndahl, T. Growth Kinetics, Properties, Performance, and Stability of Atomic Layer Deposition Zn-Sn-O Buffer Layers for Cu(In,Ga)Se₂ Solar Cells: ALD Zn-Sn-O Buffer Layers for Cu(In,Ga)Se₂ Solar Cells. *Prog Photovolt Res Appl* **2012**, *20* (7), 883–891. <https://doi.org/10.1002/pip.1153>.
 - (18) Hashimoto, Y.; Kohara, N.; Negami, T.; Nishitani, N.; Wada, T. Chemical Bath Deposition of Cds Buffer Layer for GIGS Solar Cells. *Sol. Energy Mater. Sol. Cells* **1998**, *50* (1–4), 71–77. [https://doi.org/10.1016/S0927-0248\(97\)00124-4](https://doi.org/10.1016/S0927-0248(97)00124-4).
 - (19) Kokotov, M.; Hodes, G. Reliable Chemical Bath Deposition of ZnO Films with Controllable Morphology from Ethanolamine-Based Solutions Using KMnO₄ Substrate Activation. *J Mater Chem* **2009**, *19* (23), 3847. <https://doi.org/10.1039/b821242b>.
 - (20) Taunk, P. B.; Das, R.; Bisen, D. P.; Tamrakar, R. K.; Rathor, N. Synthesis and Optical Properties of Chemical Bath Deposited ZnO Thin Film. *Karbala Int. J. Mod. Sci.* **2015**, *1* (3), 159–165. <https://doi.org/10.1016/j.kijoms.2015.11.002>.
 - (21) Govender, K.; Boyle, D. S.; Kenway, P. B.; O'Brien, P. Understanding the Factors That Govern the Deposition and Morphology of Thin Films of ZnO from Aqueous Solution. *J Mater Chem* **2004**, *14* (16), 2575–2591. <https://doi.org/10.1039/B404784B>.
 - (22) Baviskar, P. K.; Nikam, P. R.; Gargote, S. S.; Ennaoui, A.; Sankapal, B. R. Controlled Synthesis of ZnO Nanostructures with Assorted Morphologies via Simple Solution

- Chemistry. *J. Alloys Compd.* **2013**, *551*, 233–242.
<https://doi.org/10.1016/j.jallcom.2012.10.052>.
- (23) Edinger, S.; Bansal, N.; Bauch, M.; Wibowo, R. A.; Hamid, R.; Trimmel, G.; Dimopoulos, T. Comparison of Chemical Bath-Deposited ZnO Films Doped with Al, Ga and In. *J Mater Sci* **2017**, *52* (16), 9410–9423. <https://doi.org/10.1007/s10853-017-1104-8>.
- (24) Fu, X.; Wang, X.; Ding, Z.; Leung, D. Y. C.; Zhang, Z.; Long, J.; Zhang, W.; Li, Z.; Fu, X. Hydroxide ZnSn(OH)₆: A Promising New Photocatalyst for Benzene Degradation. *Appl. Catal. B Environ.* **2009**, *91* (1–2), 67–72.
<https://doi.org/10.1016/j.apcatb.2009.05.007>.
- (25) He, Q.; Zi, J.; Huang, B.; Yan, L.; Fa, W.; Li, D.; Zhang, Y.; Gao, Y.; Zheng, Z. Controlled Growth and Thermal Decomposition of Well-Dispersed and Uniform ZnSn(OH)₆ Submicrocubes. *J. Alloys Compd.* **2014**, *607*, 193–197.
<https://doi.org/10.1016/j.jallcom.2014.03.034>.
- (26) Joo, J.; Chow, B. Y.; Prakash, M.; Boyden, E. S.; Jacobson, J. M. Face-Selective Electrostatic Control of Hydrothermal Zinc Oxide Nanowire Synthesis. *Nat. Mater* **2011**, *10* (8), 596–601. <https://doi.org/10.1038/nmat3069>.
- (27) Peiró, A. M.; Ayllón, J. A.; Peral, J.; Domènech, X.; Domingo, C. Microwave Activated Chemical Bath Deposition (MW-CBD) of Zinc Oxide: Influence of Bath Composition and Substrate Characteristics. *J. Cryst. Growth* **2005**, *285* (1–2), 6–16.
<https://doi.org/10.1016/j.jcrysgro.2005.07.028>.
- (28) Wang, X.; Zhu, X.; Tao, T.; Leng, B.; Xu, W.; Mao, L. Structural Inheritance and Change from ZnSn(OH)₆ to ZnSnO₃ Compounds Used for Ethanol Sensors: Effects of Oxygen Vacancies, Temperature and UV on Gas-Sensing Properties. *J. Alloys Compd.* **2020**, *829*, 154445. <https://doi.org/10.1016/j.jallcom.2020.154445>.
- (29) Zhou, W.; Liu, Y.; Yang, Y.; Wu, P. Band Gap Engineering of SnO₂ by Epitaxial Strain: Experimental and Theoretical Investigations. *J Phys Chem C* **2014**, *118* (12), 6448–6453. <https://doi.org/10.1021/jp500546r>.
- (30) Al-Gaashani, R.; Radiman, S.; Tabet, N.; Daud, A. R. Optical Properties of SnO₂ Nanostructures Prepared via One-Step Thermal Decomposition of Tin (II) Chloride Dihydrate. *Mater. Sci. Eng. B* **2012**, *177* (6), 462–470.
<https://doi.org/10.1016/j.mseb.2012.02.006>.
- (31) Wahila, M. J.; Lebens-Higgins, Z. W.; Butler, K. T.; Fritsch, D.; Treharne, R. E.; Palgrave, R. G.; Woicik, J. C.; Morgan, B. J.; Walsh, A.; Piper, L. F. J. Accelerated Optimization of Transparent, Amorphous Zinc-Tin-Oxide Thin Films for Optoelectronic Applications. *APL Mater.* **2019**, *7* (2), 022509. <https://doi.org/10.1063/1.5053683>.
- (32) Mullings, M. N.; Hägglund, C.; Tanskanen, J. T.; Yee, Y.; Geyer, S.; Bent, S. F. Thin Film Characterization of Zinc Tin Oxide Deposited by Thermal Atomic Layer Deposition. *Thin Solid Films* **2014**, *556*, 186–194.
<https://doi.org/10.1016/j.tsf.2014.01.068>.
- (33) Thirumoorthi, M.; Thomas Joseph Prakash, J. Doping Effects on Physical Properties of (1 0 1) Oriented Tin Zinc Oxide Thin Films Prepared by Nebulizer Spray Pyrolysis Method. *Mater. Sci. Eng. B* **2019**, *248*, 114402.
<https://doi.org/10.1016/j.mseb.2019.114402>.
- (34) Homnan, S.; Malison, P.; Amratisha, K.; Kanjanaboos, P.; Wongratanaphisan, D.; Sagawa, T.; Ruankham, P. Low-Temperature Processable Sn-Doped ZnO Films as Electron Transporting Layers for Perovskite Solar Cells. *J Mater Sci Mater Electron* **2021**, *32* (23), 27279–27289. <https://doi.org/10.1007/s10854-021-07097-6>.
- (35) Dhara, S.; Niang, K.; Flewitt, A.; Nathan, A.; Lynch, S. Tail-States Induced Appearance of Conductor-like Behaviour in Zinc-tin-oxide Photo-thin-film Transistors under Sub-Bandgap Light Excitation. **2021**. <https://doi.org/10.21203/rs.3.rs-540352/v1>.

- (36) Yang, B. S.; Oh, S.; Kim, Y. J.; Han, S. J.; Lee, H. W.; Kim, H. J.; Kim, S.; Park, H. K.; Heo, J.; Jeong, J. K.; Kim, H. J. The Anomalous Effect of Oxygen Ratio on the Mobility and Photobias Stability of Sputtered Zinc–Tin–Oxide Transistors. *IEEE Trans Electron Devices* **2014**, *61* (6), 2071–2077. <https://doi.org/10.1109/TED.2014.2318055>.
- (37) Biswas, A.; Saha, S.; Jana, N. R. ZnSnO₃ Nanoparticle-Based Piezocatalysts for Ultrasound-Assisted Degradation of Organic Pollutants. *ACS Appl. Nano Mater.* **2019**, *2* (2), 1120–1128. <https://doi.org/10.1021/acsanm.9b00107>.
- (38) Zatsépin, D. A.; Boukhvalov, D. W.; Kurmaev, E. Z.; Zhidkov, I. S.; Kim, S. S.; Cui, L.; Gavrilov, N. V.; Cholakh, S. O. XPS and DFT Study of Sn Incorporation into ZnO and TiO₂ Host Matrices by Pulsed Ion Implantation: XPS and DFT Study of Sn Incorporation into ZnO and TiO₂. *Phys Status Solidi B* **2015**, *252* (8), 1890–1896. <https://doi.org/10.1002/pssb.201552145>.
- (39) Wang, Y.-T.; Chang, K.-S. Piezopotential-Induced Schottky Behavior of Zn_{1-x}SnO₃ Nanowire Arrays and Piezophotocatalytic Applications. *J. Am. Ceram. Soc.* **2016**, *99* (8), 2593–2600. <https://doi.org/10.1111/jace.14264>.
- (40) Kwoka, M.; Ottaviano, L.; Passacantando, M.; Santucci, S.; Czempik, G.; Szuber, J. XPS Study of the Surface Chemistry of L-CVD SnO₂ Thin Films after Oxidation. *Thin Solid Films* **2005**, *490* (1), 36–42. <https://doi.org/10.1016/j.tsf.2005.04.014>.
- (41) Cai, S.; Li, Y.; Chen, X.; Ma, Y.; Liu, X.; He, Y. Optical and Electrical Properties of Ta-Doped ZnSnO₃ Transparent Conducting Films by Sol–Gel. *J. Mater. Sci. Mater. Electron.* **2016**, *27* (6), 6166–6174. <https://doi.org/10.1007/s10854-016-4544-z>.
- (42) Kwoka, M.; Krzywiecki, M. Impact of Air Exposure and Annealing on the Chemical and Electronic Properties of the Surface of SnO₂ Nanolayers Deposited by Rheotaxial Growth and Vacuum Oxidation. *Beilstein J. Nanotechnol.* **2017**, *8*, 514–521. <https://doi.org/10.3762/bjnano.8.55>.
- (43) Lee, S.-H.; Kwon, K.; Kim, K.; Yoon, J. S.; Choi, D.-S.; Yoo, Y.; Kim, C.; Kang, S.; Kim, J. H. Electrical, Structural, Optical, and Adhesive Characteristics of Aluminum-Doped Tin Oxide Thin Films for Transparent Flexible Thin-Film Transistor Applications. *Materials* **2019**, *12* (1), 137. <https://doi.org/10.3390/ma12010137>.
- (44) Al-Hinai, A. T.; Al-Hinai, M. H.; Dutta, J. Application of Eh-PH Diagram for Room Temperature Precipitation of Zinc Stannate Microcubes in an Aqueous Media. *Mater. Res. Bull.* **2014**, *49*, 645–650. <https://doi.org/10.1016/j.materresbull.2013.10.011>.
- (45) Awan, S. U.; Hasanain, S. K.; Bertino, M. F.; Jaffari, G. H. Effects of Substitutional Li on the Ferromagnetic Response of Li Co-Doped ZnO:Co Nanoparticles. *J. Phys. Condens. Matter* **2013**, *25* (15), 156005. <https://doi.org/10.1088/0953-8984/25/15/156005>.
- (46) Hultqvist, A.; Edoff, M.; Törndahl, T. Evaluation of Zn Sn O Buffer Layers for CuIn_{0.5}Ga_{0.5}Se₂ Solar Cells. *Prog Photovolt Res Appl* **2011**, *19* (4), 478–481. <https://doi.org/10.1002/pip.1039>.
- (47) Lindahl, J. Atomic Layer Deposition of Zinc Tin Oxide Buffer Layers for Cu(In, Ga)Se₂ Solar Cells. PhD Thesis, Acta Universitatis Upsaliensis, Uppsala, 2015.
- (48) Green, M. A. *Solar Cells: Operating Principles, Technology, and System Applications*; Prentice-Hall, Inc., Englewood Cliffs, NJ, 1982.
- (49) Fu, Y.; Sáez-Araoz, R.; Köhler, T.; Krüger, M.; Steigert, A.; Lauermann, I.; Lux-Steiner, M. Ch.; Fischer, C.-H. Spray-ILGAR ZnS Nanodots/In₂S₃ as Defect Passivation/Point Contact Bilayer Buffer for Cu(In,Ga)(S,Se)₂ Solar Cells. *Sol. Energy Mater. Sol. Cells* **2013**, *117*, 293–299. <https://doi.org/10.1016/j.solmat.2013.06.007>.
- (50) Sozzi, G.; Di Napoli, S.; Menozzi, R.; Bissig, B.; Buecheler, S.; Tiwari, A. N. Impact of Front-Side Point Contact/Passivation Geometry on Thin-Film Solar Cell Performance. *Sol. Energy Mater. Sol. Cells* **2017**, *165*, 94–102. <https://doi.org/10.1016/j.solmat.2017.02.031>.

- (51) Fuster, D.; Anacleto, P.; Virtuoso, J.; Zutter, M.; Brito, D.; Alves, M.; Aparicio, L.; Fuertes Marrón, D.; Briones, F.; Sadewasser, S.; García, J. M. System for Manufacturing Complete Cu(In,Ga)Se₂ Solar Cells in Situ under Vacuum. *Sol. Energy* **2020**, *198*, 490–498. <https://doi.org/10.1016/j.solener.2020.01.073>.
- (52) Lehmann, J.; Lehmann, S.; Lauermann, I.; Rissom, T.; Kaufmann, C. A.; Lux-Steiner, M. Ch.; Bär, M.; Sadewasser, S. Reliable Wet-Chemical Cleaning of Natively Oxidized High-Efficiency Cu(In,Ga)Se₂ Thin-Film Solar Cell Absorbers. *J. Appl. Phys.* **2014**, *116* (23), 233502. <https://doi.org/10.1063/1.4903976>.
- (53) Colombara, D.; Elanzeery, H.; Nicoara, N.; Sharma, D.; Claro, M.; Schwarz, T.; Koprek, A.; Wolter, M. H.; Melchiorre, M.; Sood, M.; Valle, N.; Bondarchuk, O.; Babbe, F.; Spindler, C.; Cojocaru-Miredin, O.; Raabe, D.; Dale, P. J.; Sadewasser, S.; Siebentritt, S. Chemical Instability at Chalcogenide Surfaces Impacts Chalcopyrite Devices Well beyond the Surface. *Nat Commun* **2020**, *11* (1), 3634. <https://doi.org/10.1038/s41467-020-17434-8>.
- (54) Salvador, Paulo Miguel Babo Cunha. Deposition and Characterization of CdS and ZnO:Al Thin Films for Cu(In,Ga)Se Solar Cells. Master Thesis, Universidade do Minho, Braga, Portugal, 2017. <https://hdl.handle.net/1822/45504>.
- (55) Zanatta, A. R. Revisiting the Optical Bandgap of Semiconductors and the Proposal of a Unified Methodology to Its Determination. *Sci. Rep.* **2019**, *9* (1), 11225. <https://doi.org/10.1038/s41598-019-47670-y>.
- (56) Tauc, J. Optical Properties and Electronic Structure of Amorphous Ge and Si. *Mater. Res. Bull.* **1968**, *3* (1), 37–46. [https://doi.org/10.1016/0025-5408\(68\)90023-8](https://doi.org/10.1016/0025-5408(68)90023-8).

Supporting Information

Chemical bath deposition of $\text{Zn}_{1-x}\text{Sn}_x\text{O}_y$ films as buffer layers for $\text{Cu}(\text{In,Ga})\text{Se}_2$ solar cells

Diego A. Garzón, Christian Rossi, Ishwor Khatri, Francesco Soggia, Ihsan Çaha, Francis Leonard Deepak, Diego Colombara, Sascha Sadewasser*

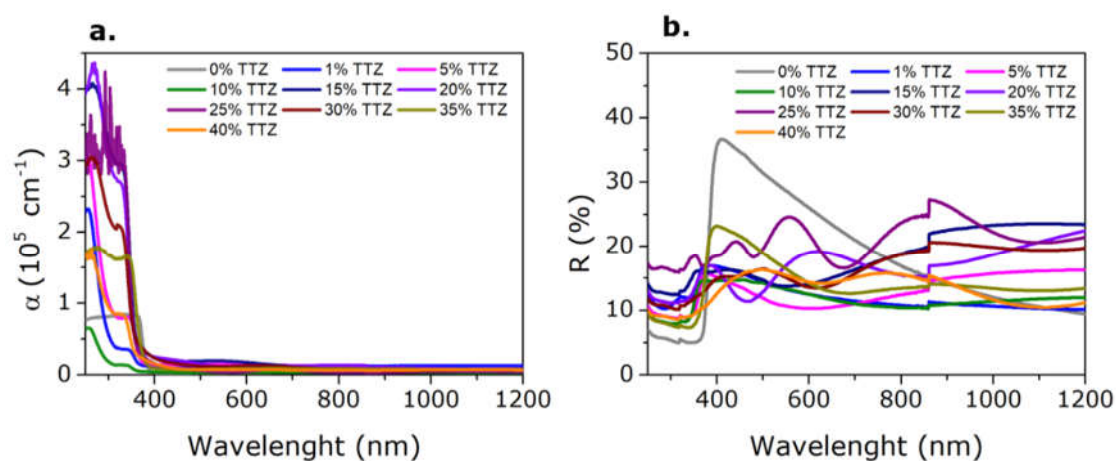


Figure S1. (a) Absorption and (b) reflectance spectra of ZTO films.

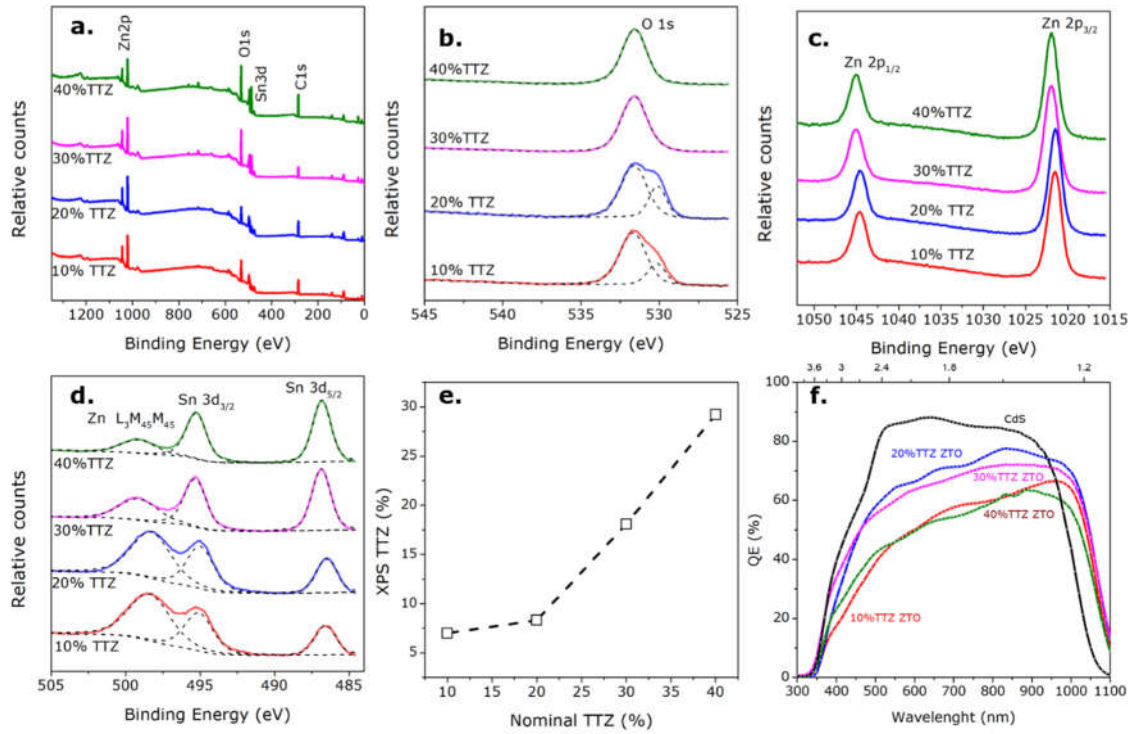


Figure S2. (a) Survey XPS spectra of ZTO thin films on CIGSe, and (b) high-resolution XPS peaks of O 1s, (c) Zn 2p, (d) and Sn 3d. The dashed lines show the fitting. (e) XPS TTZ_{film} as a function of TTZ. (f) EQE spectra for the champion cells of the 10-40% TTZ ZTO-based and CdS-based devices. The CdS spectrum indicated a different E_g for the absorber, which we attributed to the fact that different pieces from the same industrially processed CIGSe were used.

Table S1. Sn 3d_{5/2} XPS peak position comparison with the literature.

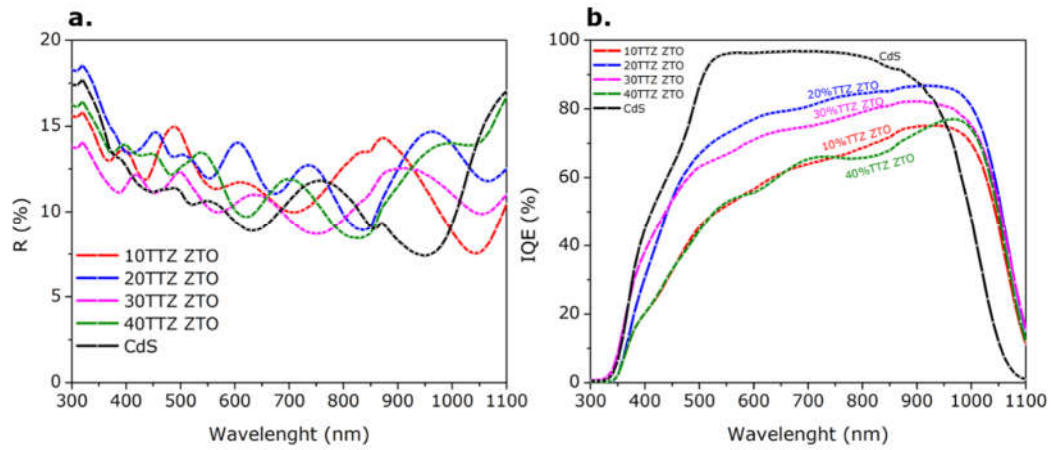
Material	Sn ²⁺ 3d _{5/2} [eV]	Sn ⁴⁺ 3d _{5/2} [eV]	Ref.
SnO ₂ deposited by Laser chemical vapor deposition (L-CVD)	485.9	486.6	1
ZnSnO ₃ sol-gel spin coated	485.69	486.34	2
SnO ₂ nanolayers deposited by rheotaxial growth and vacuum oxidation	486.06	487.2	3
Al-doped SnO _x films deposited via reactive co-sputtering	486.3	487.0	4
Average	486.0	486.8	-
Zn_{1-x}Sn_xO_y by CBD	486.68		This work

Table S2. Parameters of the champion cells for each sample.

Parameter	CdS	10% TTZ ZTO	20% TTZ ZTO	30% TTZ ZTO	40% TTZ ZTO
Jsc [mA cm ⁻²]	36	25	30	29	22
Voc [mV]	599	435	539	482	434
FF [%]	63	53	65	63	44
PCE [%]	13.6	5.6	10.4	8.6	4.2
Series resistance [Ω cm ²]	0.8	3.3	1.8	1.1	6.0
Shunt resistance [Ω cm ²]	126	131	421	248	90

Table S3. Average parameters for each solar cell.

Parameter	CdS	10% TTZ ZTO	20% TTZ ZTO	30% TTZ ZTO	40% TTZ ZTO
Jsc [mA cm ⁻²]	29±4	22±1	28±1	27±1	20±2
Voc [mV]	598±9	404±19	528±21	466±9	411±16
FF [%]	67±6	50±4	56±8	54±6	32±7
PCE [%]	11±2	4±1	9±2	7±1	3±1
Series resistance [Ω cm ²]	0.8±0.3	4±1	3±1	2±1	22±12
Shunt resistance [Ω cm ²]	657±369	108±22	225±133	151±53	48±21

**Figure S3.** (a) Reflectance spectra of the CdS- and ZTO-based solar cells and (b) internal quantum efficiency obtained by normalizing the EQE with respect to the reflectance.

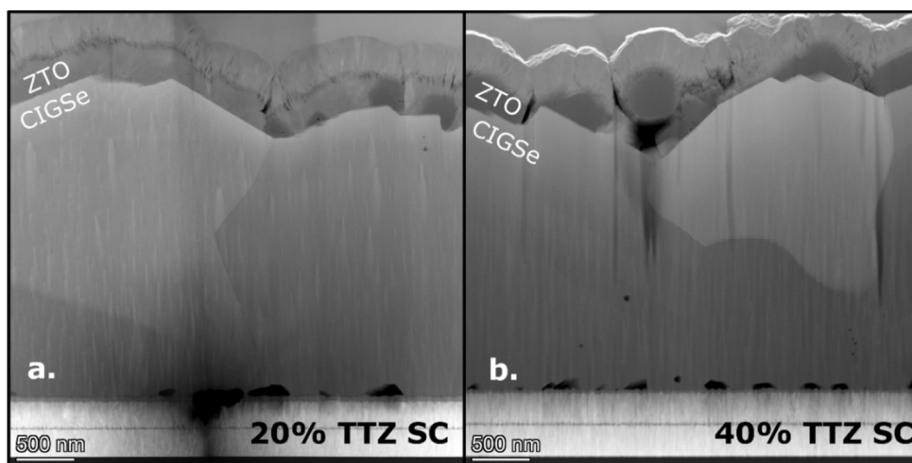


Figure S4. HAADF STEM images of lamellae extracted from the ZTO based solar cells with a buffer layer of (a) 20% and (b) 40% TTZ

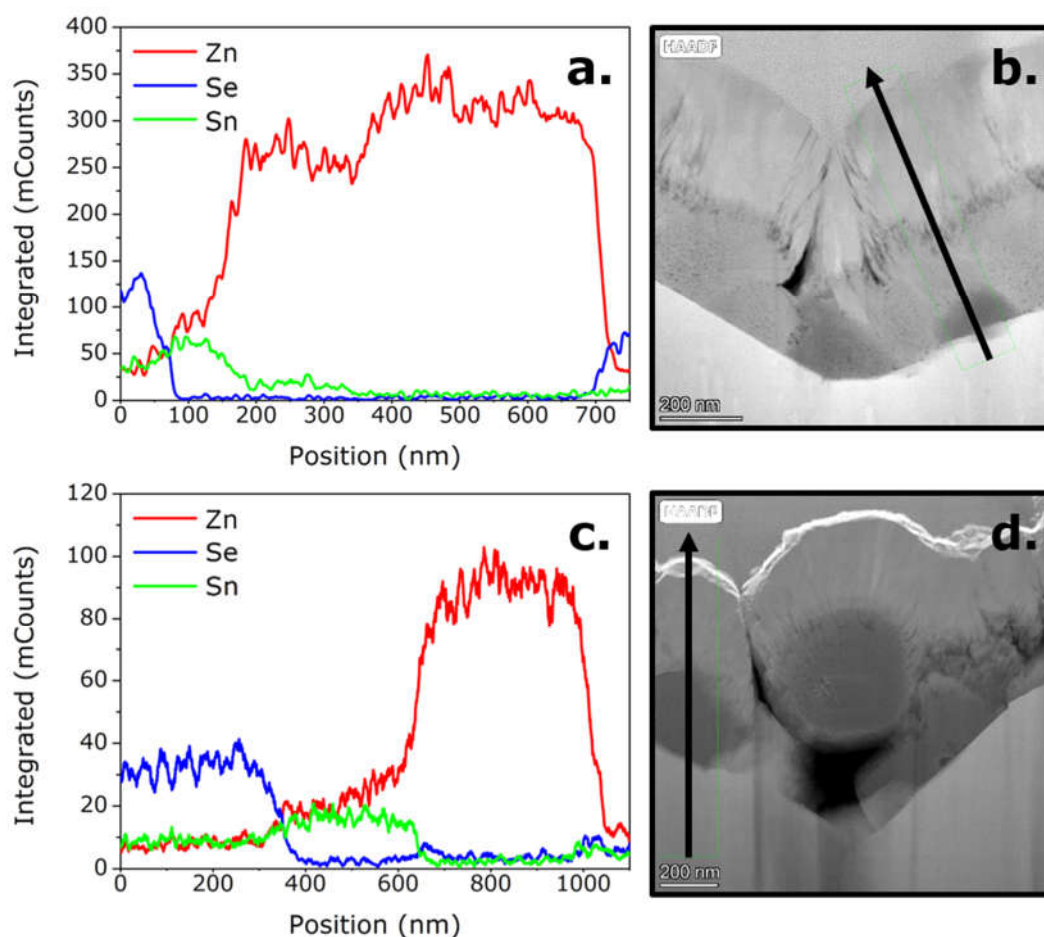


Figure S5. HAADF STEM images of lamellae extracted from the ZTO based solar cells, together with the respective line profiles of Zn (red), Sn (green), Se (blue) across the CIGS/ZTO/ZnMgO/ZnO:Al interface as indicated by the vertical arrow for buffer layer of (a, b) 20% and (c, d) 40% TTZ.

References

- [1] Kwoka, M.; Ottaviano, L.; Passacantando, M.; Santucci, S.; Czempik, G.; Szuber, J. *Thin Solid Films* **2005**, *490* (1), 36–42.
- [2] Al-Gaashani, R.; Radiman, S.; Tabet, N.; Daud, A. R. *Mater. Sci. Eng. B* **2012**, *177* (6), 462–470.
- [3] Kwoka, M.; Krzywiecki, M. *Beilstein J. Nanotechnol.* **2017**, *8*, 514–521.
- [4] Lee, S.-H.; Kwon, K.; Kim, K.; Yoon, J. S.; Choi, D.-S.; Yoo, Y.; Kim, C.; Kang, S.; Kim, J. H. *Materials* **2019**, *12* (1), 137.